

See discussions, stats, and author profiles for this publication at: <https://www.researchgate.net/publication/243374944>

Hematite with the Urchinlike Structure: Its Shape-Selective Synthesis, Magnetism, and Enhanced Photocatalytic Performance after TiO₂ Encapsulation

ARTICLE in THE JOURNAL OF PHYSICAL CHEMISTRY C · JANUARY 2010

Impact Factor: 4.77 · DOI: 10.1021/jp909111j

CITATIONS

34

READS

14

4 AUTHORS, INCLUDING:



Suyuan Zeng

Liaocheng University

46 PUBLICATIONS 780 CITATIONS

SEE PROFILE



Kaibin Tang

University of Science and Technology of C...

204 PUBLICATIONS 4,181 CITATIONS

SEE PROFILE

Hematite with the Urchinlike Structure: Its Shape-Selective Synthesis, Magnetism, and Enhanced Photocatalytic Performance after TiO₂ Encapsulation

Suyuan Zeng,^{†,‡} Kaibin Tang,^{*,†} Tanwei Li,[†] and Zhenhua Liang[†]

Nanomaterial and Nanochemistry, Hefei National Laboratory for Physical Sciences at Microscale, University of Science and Technology of China, Hefei, Anhui, 230026, P. R. China, and College of Chemistry and Chemical Engineering, Liaocheng University, Liaocheng, Shandong, 252059, P. R. China

Received: September 22, 2009; Revised Manuscript Received: November 12, 2009

In this work, a facile route using simple a hydrothermal reaction and sequential calcinations for the selective synthesis of 3D α -Fe₂O₃ urchinlike nanostructures without employing templates or matrixes is presented. By hydrolyzing FeCl₃ in the solution containing different anions (SO₄²⁻, Cl⁻, NO₃⁻, ClO₃⁻, ClO₄⁻, C₂O₄²⁻, Br⁻), product with certain morphology can be selectively synthesized. The effect of inorganic anions on the morphologies and sizes of the products was systematically investigated. A probable formation mechanism for the urchinlike nanostructure was proposed. Magnetic hysteresis measurements of the as-obtained products reveal that magnetic properties of products were shape-dependent. The as-obtained α -Fe₂O₃ nanostructures show photocatalytic activity on the decomposition of RhB upon irradiation by the UV light. The photocatalytic performance can be further enhanced by TiO₂ coating.

1. Introduction

The fabrication of complex nanoarchitectures with controlled morphology, orientation, and dimensionality have attracted significant attention over the past decade because such control is crucial for the determination of structure–property relationships in many processes, development of new pathways for the materials synthesis, and novel applications of nanostructured materials.^{1–4} For this purpose, these years, a large number of nanomaterials with complex structures has been successfully prepared through various methods, such as ZnS nanoflowers by the CVD method,⁵ Bi₂Te₃ nanotube arrays by the template-assisted method,⁶ In₂O₃ nanoflowers by the solvothermal method,⁷ and nickel nanostructures assembled by nanoplatelets using the hydrothermal technique.⁸ Among these compounds, much attention has been focused on hematite (α -Fe₂O₃) nanostructures because of its application in various fields, such as catalysts, pigments, and sensors.^{9–11} As a result, hematite possessing various morphologies, such as spheres, cubes, ellipsoids, spindles, disks, hexagonal platelets, peanuts, rods, wires, and belts has been successfully prepared.¹² However, it is still a big challenge to develop simple and reliable synthetic methods to assemble these low-dimensional building blocks into complex 3D ordered nanostructures with designed chemical components and controlled morphologies, which will strongly affect the properties of nanomaterials.

These years, continuous efforts have been made on the preparation of hematite 3D nanostructures due to their promising applications in many fields. For example, by oxidizing the Fe substrate, Yang's group has succeeded in preparing α -Fe₂O₃ nanobelts and nanorod arrays.¹³ By the reaction of Fe powder with water vapor, Zhu's group also succeeded in the preparation of α -Fe₂O₃ nanobelt and nanowire arrays on the surface of the Fe powder.¹⁴ Besides the CVD method, the template-assisted

method has also been widely employed in the preparation of α -Fe₂O₃ nanostructures. Using AAO membrane as the template, Xue and co-workers successfully prepared α -Fe₂O₃ nanowire array.¹⁵ Yue's group also prepared the α -Fe₂O₃ nanowire arrays by using SBA15 as a template.¹⁶ However, 3D nanoarchitectures prepared by template or CVD method usually suffer from disadvantages relating to high cost and tedious procedures, which may prevent them from being used in large-scale applications. Thus, one would prefer some more facile and economic method for the preparation of the hematite 3D nanostructures. Given the reasons mentioned above, these years, many solution-based methods such as the hydrothermal and solvothermal methods were brought into the synthesis of α -Fe₂O₃ 3D nanoarchitectures. Using the mixed solution of ethylene glycol and water as the reaction medium, Yang and co-workers also succeeded in the synthesis of airplane-like α -Fe₂O₃ nanostructures.¹⁷ Wan's group reported the preparation of α -Fe₂O₃ nanoflowers by using ethylene glycol as the solvent.¹⁸ Zhang and co-workers have also succeeded in the synthesis of α -Fe₂O₃ nanoflowers through the solvothermal method by employing isopropanol as the solvent.¹⁹ Considering the side effects caused by the use of organic solvents, hydrothermal reactions would be more preferred. By treating K₃[Fe(CN)₆] in aqueous solution at 140 °C, Hu's group succeeded in the preparation of single-crystal dendritic micropines of α -Fe₂O₃.²⁰ Fu's group reported the template-free synthesis of the urchinlike hematite nanostructures.²¹ Recently, Yu's group has also succeeded in the preparation of hierarchical hematite nanorings by the simple hydrothermal method.²² However, it still remains a great challenge for the selective synthesis among different 3D α -Fe₂O₃ nanoarchitectures, which will facilitate our understanding of the shape-dependent properties of the products.

It is well-known that some organic molecules, such as surfactant and polymer electrolytes, are effective structure directing agents for morphology and size control in the synthesis procedures of various nanostructures.²³ Recently, some groups have found that the added or residual inorganic species in the

* To whom correspondence should be addressed. Tel: +86-551-3601791. Fax: +86-551-3601791. E-mail: kbtang@ustc.edu.cn (K.T.).

[†] University of Science and Technology of China.

[‡] Liaocheng University.

organic molecule-based synthesis systems also play a vital role similar to the organic molecules on controlling the morphology and size of as-synthesized nanostructures.²⁴ Therefore, the small inorganic ions can be considered as part of the structure-directing agent or even the only one. They have shown their advantages as structure-directing additives over the organic ones in terms of environmental benignity and low cost. However, there are few reports on the investigation of the roles of inorganic species in controlling the size and shape of nanostructures so far.

Most of the solution-based methods for the preparation of hematite nanostructures are based on the hydrolysis of Fe^{3+} in the solution, and this has been extensively studied by many scientists. Among them, Matijević's and Sugimoto's groups have done lots of works on the hydrolysis of iron(III) chloride. Matijević and co-workers prepared monodispersed spindle hematite using forced hydrolysis of ferric ions,^{12c} and Sugimoto et al. synthesized a series of hematite particles with controllable size and shape.²⁵ As it has been pointed by Matijević, the morphologies of the products depended on the concentration of ferric ion, pH, solvent, and the anions presented in the systems.²⁶ Thus, the selective synthesis of $\alpha\text{-Fe}_2\text{O}_3$ is possible by simply tuning the experimental parameters such as the anions present, pH, or the concentrations of the reactants. In this article, we reported the selective synthesis of $\alpha\text{-Fe}_2\text{O}_3$ urchinlike nanoarchitectures by hydrolyzing FeCl_3 in the presence of sulfate ions. The roles of the inorganic ions, pH, and the concentration of the reactants are investigated. The magnetic and photocatalytic properties of the as-obtained nanostructures are also investigated.

2. Experimental Section

All of the reagents are of analytical grade and used without any purification.

2.1. Preparation of the Sea Urchinlike $\alpha\text{-Fe}_2\text{O}_3$ Nanoarchitectures. In a typical experiment, 2 mmol iron chloride ($\text{FeCl}_3 \cdot 6\text{H}_2\text{O}$) and 2 mmol sodium sulfate (Na_2SO_4) were added into 40 mL deionized water and stirred until totally dissolved. The solution was then transferred into a 50 mL Teflon-lined stainless steel autoclave and kept at 120 °C for 6 h and then cooled naturally. The products were collected by centrifugation and washed with deionized water and absolute ethanol several times and dried in air at 60 °C for 12 h. In the next step, the as-prepared FeOOH precursors were annealed in air at 400 °C for 2 h with the heating speed of 1 °C/min. Red solids were obtained, which were collected for further analysis.

2.2. Preparation of the Sea Urchinlike $\alpha\text{-Fe}_2\text{O}_3/\text{TiO}_2$ Nanostructures. In a typical experiment, the as-obtained $\alpha\text{-Fe}_2\text{O}_3$ urchinlike nanostructures (0.1 g) was dispersed into the tetrabutyl titanate solution (dissolved in ethanol, 1 $\text{mol} \cdot \text{L}^{-1}$) under vigorous stirring and then kept still for 24 h at room temperature. The resulting product was separated by centrifugation and washed with absolute ethanol 2 times and then dispersed into deionized water under stirring. After stirring for 0.5 h, the red product was collected by centrifugation and dried in vacuum at 60 °C. In the next step, the as-prepared precursors were annealed in air at 200 and 390 °C for 2 h with a heating speed of 1 °C/min. Red solids were obtained, which were collected for further analysis.

2.3. Characterizations. All of the products were characterized by X-ray diffraction (XRD) on a Philips X'pert Pro SUPER rotation anode with $\text{Cu K}\alpha$ radiation ($\lambda = 1.541874 \text{ \AA}$). A scan rate of $0.0167^\circ \cdot \text{s}^{-1}$ was applied to record the pattern in the 2θ range of 10–70°. The size and the morphology of the product were observed on a SIRION FEI field emission scanning

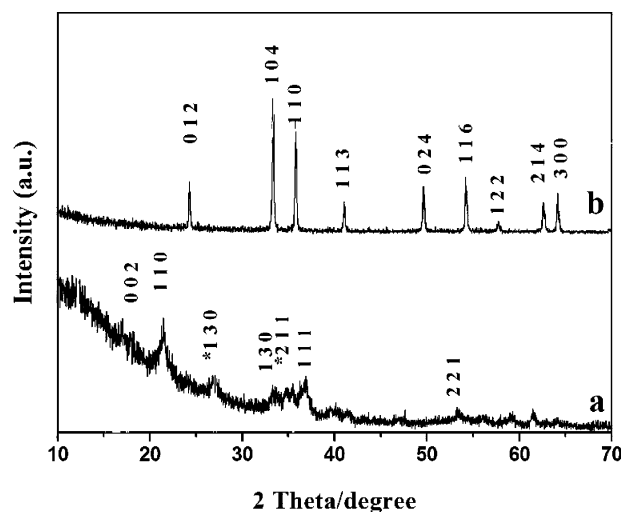


Figure 1. XRD pattern of the (a) precursor obtained by hydrolyzing Fe^{3+} ion in the Na_2SO_4 solution at 120 °C for 6 h, (b) the product obtained by calcining the precursor at 400 °C for 2 h in the air.

electronic microscopy (FESEM) equipped with a GENESIS4000 energy dispersive X-ray spectroscopy. The transmission electron microscopy (TEM) image and selected area electron diffraction was taken on a Hitachi H-800 transmission microscopy using an accelerating voltage of 200 KV. The selected area electron diffraction (SAED) patterns and high-resolution transmission electron microscopy (HRTEM) images were obtained on a JEOL-2010 TEM at an acceleration voltage of 200 KV. The Brunauer–Emmett–Teller (BET) tests were determined via a Micromeritics ASAP-2000 nitrogen adsorption apparatus. The magnetic measurements were recorded on a SQUID magnetometer, Quantum Design MPMS.

2.4. Photocatalysis Experiments. To evaluate the photocatalytic activity of our product, we compared it with other common samples. In a typical process, 50 mg of the samples was added to 100 mL of a $1.0 \times 10^{-5} \text{ M}$ Rhodamine B (RB) solution and then magnetically stirred in the dark for 15 min, which allowed it to reach adsorption equilibrium and uniform dispersity. The solution was then exposed to UV irradiation from a 250 W high-pressure Hg lamp at room temperature. The samples were collected by centrifugation every 10 min to measure the RB degradation by UV–vis spectra (Shimadzu UV2550).

3. Results and Discussion

3.1. Characterization of the Sea Urchinlike Precursor and $\alpha\text{-Fe}_2\text{O}_3$. The phase purity of the as-prepared product was examined by the X-ray diffraction (XRD). Part a of Figure 1 is the XRD pattern of the FeOOH with urchinlike morphology prepared by reacting at 120 °C for 6 h, where all the diffraction peaks on the pattern a can be indexed as orthorhombic $\alpha\text{-FeOOH}$ (JCPDS card, No. 81–0464) and tetragonal-phased FeOOH (marked with as asterisk, JCPDS card, No. 75–1594). Part b of Figure 1 is the XRD pattern of the product obtained by calcining the precursor at 400 °C for 2 h in the air, where all of the diffraction peaks can be indexed as the hexagonal $\alpha\text{-Fe}_2\text{O}_3$ with lattice constants of $a = 0.5026 \text{ nm}$ and $c = 1.3771 \text{ nm}$, which agrees well with the literature (JCPDS card, No. 33–0664). The composition of the $\alpha\text{-Fe}_2\text{O}_3$ nanostructure was further confirmed by the EDS (Figure S1 of the Supporting Information). The EDS result shows that the atom ratios of Fe-to-O are 42:58 for the obtained product, which agree well with the value calculated from the formula of hematite.

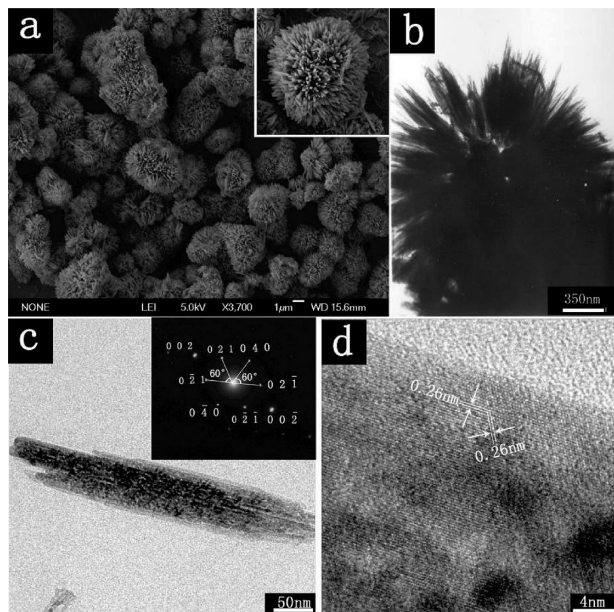


Figure 2. (a) Low-magnification FESEM images of the as-obtained precursor (insert: high-magnification FESEM image of a single nanostructure), (b) TEM image of a single sea urchin-like nanostructure, (c) TEM image of a single nanoneedle from the sea urchin-like nanostructure (insert: SAED pattern taken from the nanoneedle), (d) HRTEM image of the nanoneedle.

Field-emission scanning electron microscopy (FESEM) and transmission electron microscopy (TEM) were employed to investigate the size and morphology of the product. Part a of Figure 2 is the FESEM image of the sea urchin-like precursor, which clearly demonstrates that the precursor was composed of sea urchin-like nanostructures. Careful observation (insert of part a of Figure 2) of a single urchin-like structure shows that the urchin-like structure has a diameter of ca. $4\ \mu\text{m}$ with acicular crystallites radiating from the center in a uniform size distribution. The nanoneedles grown from the center have uniform diameters of about 150 nm and length up to 800 nm. The result agrees well with TEM image of the precursor (part b of Figure 2). Part c of Figure 2 is the TEM image of a single nanoneedle from the sea urchin-like nanostructure, indicating that the average length of the nanoneedle is about 400 nm, with a diameter of about 50 nm. What is more, by careful observation of the nanoneedles, we find that most of the nanoneedles we observed have a similar size as the one shown in part c of Figure 2. Considering the fact that the size of the sea urchin-like nanostructure is twice as large as the length of the nanoneedle, we believe that these sea urchin-like nanostructures may not form by direct connection of the nanoneedles, but formed by connecting these nanoneedles to a spherical core. The insert of part c of Figure 2 is the SAED pattern of the nanoneedle, indicating the single-crystal nature of the nanoneedle growing along the $[0\ 0\ 2]$ direction, the angles between the lattice planes agrees well with the calculated value of these planes. Part d of Figure 2 is the high resolution transmission electron microscopy (HRTEM) of a single nanoneedle, in which the clear atomic lattice fringes can be seen. The nanoneedle is structurally uniform and dislocation free. The typical lattice fringe spacings, being determined to be 0.26 nm, corresponding to the $\{0\ 2\ 1\}$ lattice planes of tetragonal FeOOH. Thus, we speculate that the sea urchin-like nanostructure may be a heterostructure with the $\alpha\text{-FeOOH}$ spherical core and the tetragonal-phased FeOOH nanoneedles.

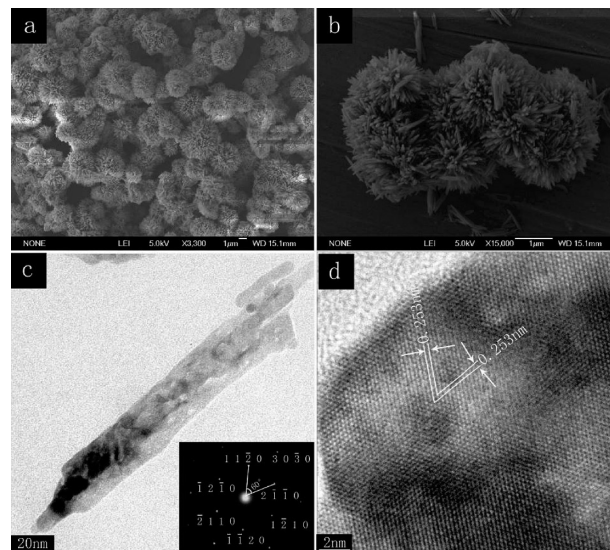


Figure 3. (a, b) Low- and high-magnification FESEM images of the sea urchin-like $\alpha\text{-Fe}_2\text{O}_3$ nanostructures, (c) TEM image of a single nanoneedle from the sea urchin-like $\alpha\text{-Fe}_2\text{O}_3$ nanostructure (insert: SAED pattern of the nanoneedle), (d) HRTEM image of selected nanoneedle.

Parts a and b of Figure 3 are the low- and high-magnification FESEM images of $\alpha\text{-Fe}_2\text{O}_3$ obtained by calcining the precursor at $400\ ^\circ\text{C}$ for 2 h in the air. The result shows that the urchin-like structure is perfectly maintained after calcination. Part c of Figure 3 is the TEM image of a single nanoneedle from the sea urchin-like $\alpha\text{-Fe}_2\text{O}_3$ nanostructure, demonstrating that the size of the $\alpha\text{-Fe}_2\text{O}_3$ nanoneedle is smaller than the corresponding precursor, which may result from the decomposition of the precursor. The insert of part c of Figure 3 is the SAED pattern of the $\alpha\text{-Fe}_2\text{O}_3$ nanoneedle, indicating the single-crystal nature of the nanorod grown along the $[1\ 0\ -1\ 0]$ direction and the angles between the lattice planes agrees well with the calculated value of these planes. Part d of Figure 3 is the corresponding HRTEM image of the nanoneedle, the typical lattice fringe spacing, being determined to be 0.253 nm, corresponding to the $\{1\ 1\ -2\ 0\}$ lattice planes of hexagonal $\alpha\text{-Fe}_2\text{O}_3$, agrees well with the diffraction pattern.

3.2. Influence of the Inorganic Anions on the Morphologies of the Precursors. When Fe^{3+} ion hydrolyzes in the water, the morphologies of the product obtained are closely related to the ions exist in the solution, such as H^+ , OH^- , and other inorganic anions. Here, the relationship between the inorganic anions and the morphologies of the precursors was systematically investigated. Keeping the pH, reaction temperature, time, and the dosage of FeCl_3 constant, Na_2SO_4 was replaced by other inorganic salt to investigate the effect of different anions on the morphologies of the precursor. When 2 mmol NaCl was used instead of Na_2SO_4 in the reaction, uniform nanorods were obtained (Figure 4). Part a of Figure 4 is the low-magnification FESEM image of the product, which clearly demonstrates that the product is composed of nanorods with uniform size and shape. These nanorods, aligned parallelly, form a small nanorod array. The high-magnification FESEM image of these nanorod arrays shows that the length of these nanorods is about 200 nm and the diameter of these nanorods is about 30 nm. Parts b and c of Figure 4 are the FESEM and TEM images of the nanorod arrays, which shows that the area of the nanorod array is not very large, the usual area is about $2 \times 2\ \mu\text{m}^2$. Part c of Figure 4 shows the TEM image of the nanorod array. Combined with the FESEM image, it is not difficult to find that these dots are

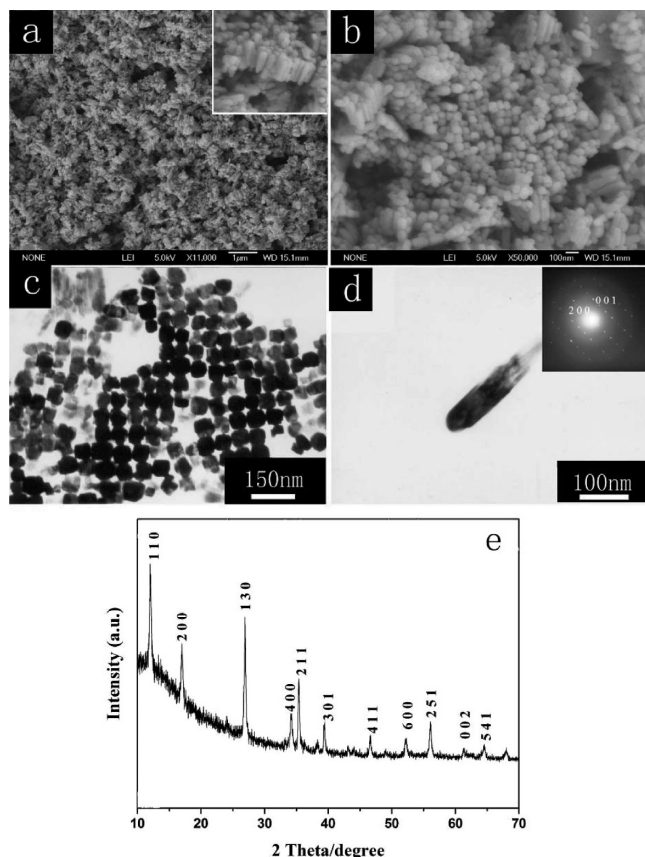


Figure 4. (a–c) FESEM and TEM images of the product obtained by replacing Na_2SO_4 with NaCl , (d) TEM image of a single nanorod (insert: SAED pattern of the selected nanorod), (e) XRD pattern of the as-obtained nanorod.

not particles but the top view of these nanorod arrays. Part e of Figure 4 is the XRD pattern of the nanorod array, where all of the diffraction peaks can be indexed as the tetragonal FeOOH (JCPDS, NO. 75–1594). Meanwhile, the selected-area electron diffraction (SAED) pattern of a single nanorod (insert of part d of Figure 4) demonstrates the single-crystal nature of the nanorod growing along the $[001]$ direction. Thus, we believe the controlled synthesis of $\alpha\text{-Fe}_2\text{O}_3$ complex nanostructures using the inorganic anion-assisted method is feasible. Then the question comes: what will the morphologies of the product be when other inorganic anions were introduced into the reaction system?

To further investigate the role of inorganic anions played in the reaction, in the next step, inorganic anions such as NO_2^- , $\text{C}_2\text{O}_4^{2-}$, ClO_3^- , ClO_4^- , CH_3COO^- , and Br^- were introduced into the reaction system instead of SO_4^{2-} . Part a of Figure 5 is the TEM image of the product obtained when 2 mmol NaNO_2 was introduced into the reaction, which shows that the product is mainly composed of nanofibers, and XRD analysis of the product shows that the as-obtained nanofibers are tetragonal-phased $\alpha\text{-FeOOH}$. When 2 mmol $\text{Na}_2\text{C}_2\text{O}_4$ was used as the starting material, the product obtained is mainly composed of solid nanospindles (part b of Figure 5), which agrees our research reported before.²⁷ Other inorganic anions such as ClO_3^- are also introduced into the reaction, and the TEM observation shows that the as-obtained product is mainly composed of nanorods with diameter of ca. 30 nm and lengths up to 250 nm (part c of Figure 5). According to Fu's report,²¹ the urchinlike hematite nanostructure could be obtained by oxidizing FeSO_4 with NaClO_3 ; here, it not difficult to see that the SO_4^{2-}

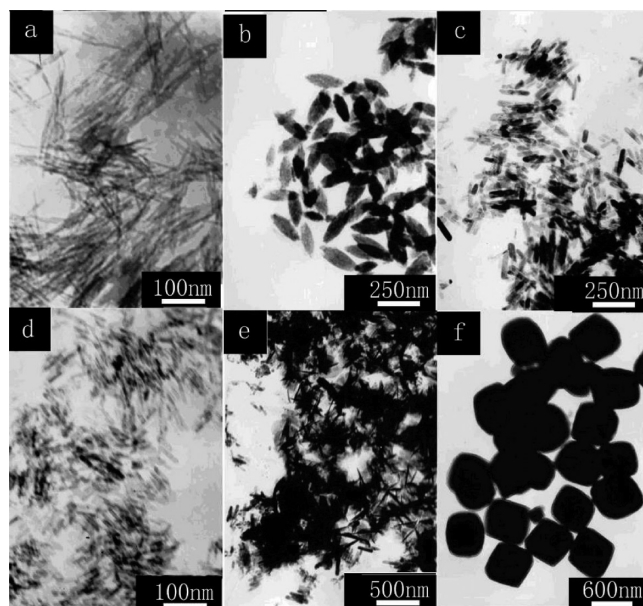


Figure 5. TEM images of the product obtained by reacting at 120 °C for 6 h when replacing Na_2SO_4 with 2 mmol (a) NaNO_2 , (b) $\text{Na}_2\text{C}_2\text{O}_4$, (c) NaClO_3 , (d) NaClO_4 , (e) NaCH_3COO , (f) NaBr .

ion plays an important role in the formation of the sea urchinlike precursor. In the next step, ClO_4^- ion, which has the same tetrahedral structure as SO_4^{2-} , is introduced into the reaction system, and TEM observation of the as-obtained product shows that the product obtained are mainly composed of nanorods, indicating that the structure of the inorganic anion is not the vital factor for the fabrication of the urchinlike nanostructures. As to the case when CH_3COO^- is introduced to the reaction, the product is mainly composed of some nanosheets. And when Br^- , which is in the same group with Cl^- , was introduced into the reaction, the product is mainly composed of nanocubes with a side length of ca. 500 nm, and XRD analysis of the product shows that the as-obtained nanocubes can be designated as hexagonal hematite. From the above experiments, it is not difficult to find that the morphologies of the product are closely related to the anions present in the solution. For the anions such as NO_2^- and $\text{C}_2\text{O}_4^{2-}$, the coordination properties may have great influence on the morphology of the product. For other anions that does not possess coordination properties, the morphology is closely related to the anions.

3.3. Influence of Inorganic Salt Dosage on the Morphologies of the Product. Because no capping agent was used in the synthesis, we believe that the amount inorganic anions plays an important role in the formation of such nanostructures. This hypothesis can be verified by our experimental data. In the first step, $(\text{NH}_4)_2\text{SO}_4$ and K_2SO_4 was used as the assistant reagent, the results show that the products obtained still have the sea urchinlike morphologies, XRD analysis of the products indicate that the products obtained are all composed of $\alpha\text{-FeOOH}$ and tetragonal FeOOH , which is in accordance with the result mentioned above. From this, we may draw the conclusion that the key factor for the fabrication of such nanostructure is the existence of inorganic anions, not the inorganic cations. Because there are two anions existing in the solution, Cl^- and SO_4^{2-} , then there is a question, which anion is vital in the formation of sea urchinlike nanostructure? To answer this question, in the next step, $\text{Fe}_2(\text{SO}_4)_3$ was used as the starting material, the SEM image of the product (shown as part a of Figure 6) shows that the product obtained still have the urchinlike morphology, and the size of the product is nearly the same as the product

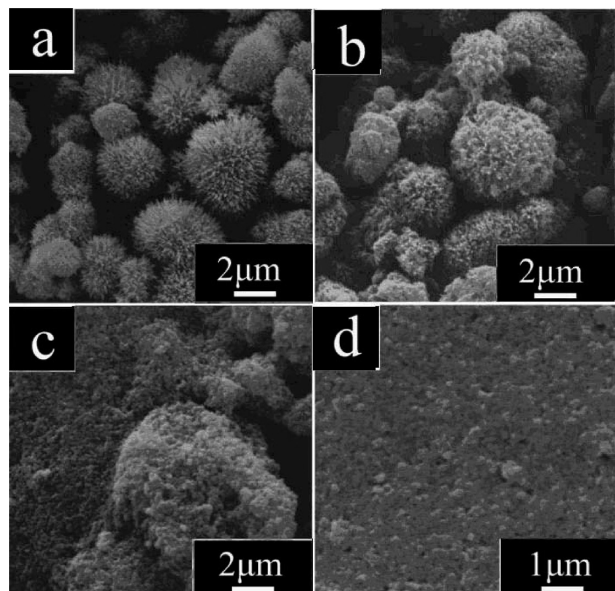


Figure 6. SEM images of the product obtained by using (a) $\text{Fe}_2(\text{SO}_4)_3$ as the starting material.

mentioned above, showing that SO_4^{2-} is key factor in the formation of the sea urchinlike nanostructure. To further investigate the relationship between the dosage of inorganic salt and the morphologies of the products, the influence of the molar ratio of inorganic anions to the Fe^{3+} on the morphology of the products in our synthetic system was studied. Keeping the dosage of Fe^{3+} and water constant, the molar ratio of inorganic anions to the Fe^{3+} was varied. When the value of $[\text{SO}_4^{2-}]/[\text{Fe}^{3+}]$ is 2, the urchinlike nanostructure are present as well as some aggregated nanoparticles (part b of Figure 6). Further increasing the value of $[\text{SO}_4^{2-}]/[\text{Fe}^{3+}]$ to 4, the SEM image (part c of Figure 6) showed that the product is composed of nanoparticles, and nearly no urchinlike nanostructures can be seen. If we continue to add more sodium sulfate to make the value of $[\text{SO}_4^{2-}]/[\text{Fe}^{3+}]$ 8, the product is totally composed of nanoparticles with diameters of about 100 nm (part d of Figure 6). As we know, the separation of nucleation and growth is the prerequisite for the formation of uniform nanostructures. It has been pointed by De Bruyn et al.²⁸ that sulfate complexes strongly with $\text{Fe}(\text{III})$ and results in complex behavior depending on the $\text{SO}_4^{2-}/\text{Fe}^{3+}$ ratio in the solutions. The presence of SO_4^{2-} results in precipitation at a greater rate than in solutions with only uninegative anions. Thus, the reaction speed becomes faster as the dosage of sulfate ion increased, causing the reaction to be kinetically control.

3.4. Influence of pH on the Morphologies of the Product.

The morphologies of the products obtained by hydrolyzing Fe^{3+} not only related to the anions present in the solution but also related to the pH of the solution, which will greatly affect the hydrolyzation speed of the Fe^{3+} . In our experiment, the effect of pH on the morphologies of the precursors was investigated. The pH of the solution before and after the reaction is measured to be 2 and 1.5, which result from the release of protons during the hydrolyzation of Fe^{3+} ions. Part a of Figure 7 is the TEM image of the precursor obtained when the pH of the solution is 1, which shows that the precursor still has the urchinlike morphology, XRD analysis of the sample further demonstrate that the product is composed of $\alpha\text{-FeOOH}$ and tetragonal-phased FeOOH , which agrees well with the result mentioned above. By tuning the pH of the solution to 7 using $1 \text{ mol} \cdot \text{L}^{-1}$ NaOH, the morphology of the precursor changed to nanorods with

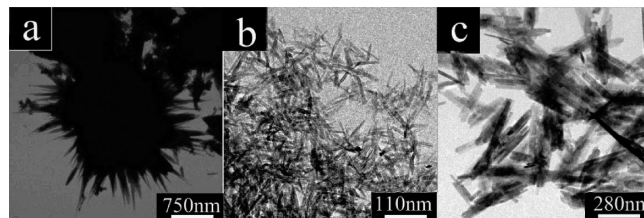


Figure 7. TEM images of the product obtained by reacting at 120°C under different pH values: (a) pH 1, (b) pH 7, and (c) pH 12.

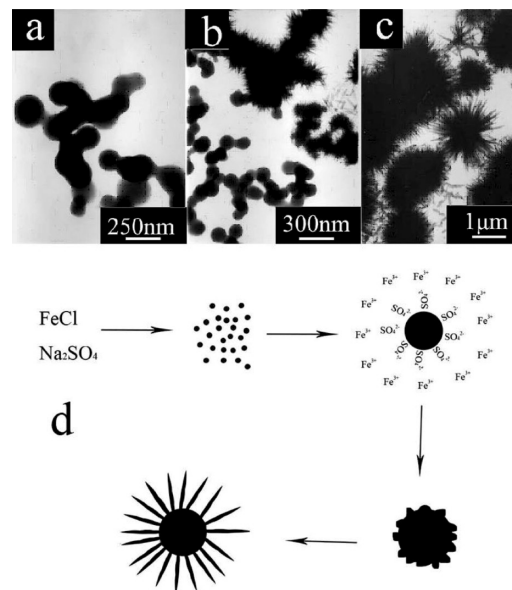


Figure 8. TEM images of the product obtained after reacting at 120°C for (a) 0.5 h, (b) 1 h, (c) 2 h, and (d) schematic diagram for the proposed growth mechanism of the sea urchinlike nanostructures.

diameter of about 10 nm and lengths up to 100 nm (part b of Figure 7). The composition of the precursor, confirmed by the XRD analysis, is designated to be $\alpha\text{-FeOOH}$. As the pH of the solution further increased to 12, the product obtained still possess the rod-like morphology with the size of the nanorods become larger as compared to the product obtained under pH 7. Concerning the previous report on the hydrolysis of Fe^{3+} , this phenomenon may result from the growing habit of $\alpha\text{-FeOOH}$.²⁹

3.5. Growth Mechanism of the Sea Urchinlike Nanostructure. To investigate the growth mechanisms of such hollow nanostructures, several experiments that involved intercepting the intermediates at different reaction times were performed. Part a of Figure 8 is the TEM image of the product obtained by reacting at 120°C for 0.5 h, which clearly demonstrates that the product is composed of some interconnected nanoparticles with a diameter of about 200 nm, and the XRD pattern of the as-obtained precursor can be indexed as the $\alpha\text{-FeOOH}$, implying the formation of the $\alpha\text{-FeOOH}$ core. Part b of Figure 8 is the TEM image of the precursor after reacting at 120°C for 1 h, which shows that the precursor is composed of some sea urchinlike nanostructures and some nanoparticles, and the average size of the sea urchinlike nanostructure is about 400 nm, which is smaller than the final product. Part c of Figure 8 is the TEM image of the precursor obtained by reacting at 120°C for 2 h, showing that the precursor is all composed of the sea urchinlike nanostructure, which is smaller in size than the final product.

On the basis of the above evolution of the time-dependent morphology, the formation process of the sea urchinlike nanostructure is illustrated as part d of Figure 8. A two-step

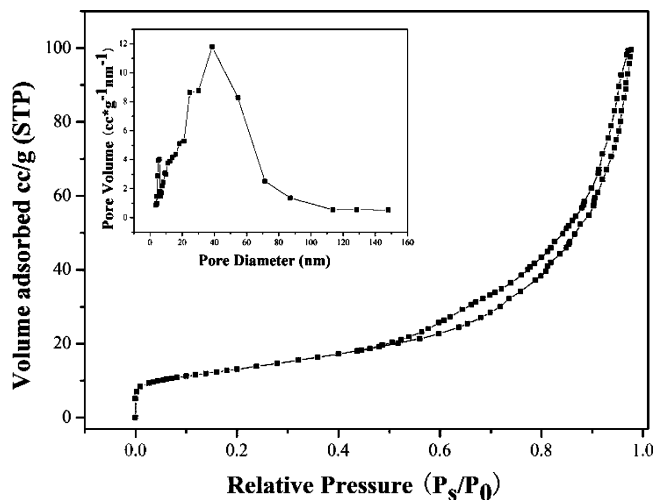


Figure 9. Nitrogen adsorption–desorption isotherm and the pore size distribution curve (insert) for the sea urchinlike α - Fe_2O_3 .

formation mechanism was proposed for the formation of the sea urchinlike nanostructure. In the initial stage, a large number of α - FeOOH nanoparticles formed in a short time through the hydrolyzation of Fe^{3+} ion, which will serve as the nuclei in the following process. Considering the acidic environment of the solution, the proton will be inevitably adsorbed on the surface of the nuclei, which will further attract the sulfate ion to form the double electric layer to stabilize the colloid. In the next step, nanoneedles will epitaxially grow along the surface of the initial nanoparticles and formed the solid urchinlike structures.

3.6. BTE Test of the Sea Urchinlike Hematite Nanostructures. Nitrogen adsorption–desorption measurement was conducted to characterize the Brunauer–Emmett–Teller (BET) surface area and internal pore superstructure. The isotherm can be categorized as type IV, with a distinct hysteresis loop observed in the range of 0.45–1.0 P/P_0 (Figure 9). The as-obtained α - Fe_2O_3 sea urchinlike nanostructure has a BET surface area of 46.850 m^2/g . The BJH analyses show that the α - Fe_2O_3 sea urchinlike nanostructure possess bimodal (small and large) mesopore distribution. The insert of Figure 9 displays main pore size distribution of ~ 25 and 41 nm in the as-obtained nanostructures, which may be formed by the aggregation of the nanoneedles, that is, the interspaces in α - Fe_2O_3 nanoneedles. Another small pore size distribution of ~ 3 nm was also observed from the BJH analysis, indicating small pores exist in all mesoporous nanoneedles composing α - Fe_2O_3 sea urchinlike nanostructures, which may formed by the removal of water from the precursor while heating. The hierarchical structured α - Fe_2O_3 with smaller and larger mesopores could reduce transport limitation in catalysis, resulting in higher activities and well-controlled selectivity.³⁰ The bimodal mesoporous α - Fe_2O_3 nanostructures may be promising applications in catalysis because their larger textural mesopores can provide reactant substances of different size transport circumstances comparable to those in open medium.³¹

3.7. Magnetic Properties of the Sea Urchinlike Nanostructures. Bulk α - Fe_2O_3 , besides the Néel temperature ($T_N = 960$ K), has a first-order magnetic transition at $T_M = 263$ K, which is called the Morin transition. Below T_M , the antiferromagnetically (AF) ordered spins are oriented along the c axis, whereas above T_M , spins lie AF in the basal plane of the crystal with a ferromagnetism component. A sharp decrease in magnetization should be observed at this transition, termed as the

Morin transition temperature (T_M). Morin temperature of α - Fe_2O_3 spherical particles was found to be strongly dependent on particle size and tends to disappear (<5 K) below a diameter of 8–20 nm.³² Our group has also reported that the disappearance of Morin transition in the porous α - Fe_2O_3 nanorods and nanoflowers, which may be attributed to the porous structure of the nanoarchitecture.³³ Thus, it would be of great interest to investigate the magnetic properties of α - Fe_2O_3 porous urchinlike nanostructures, which would facilitate our understanding of the relationship between the surface effect and the magnetic properties of α - Fe_2O_3 . For comparative purposes, the magnetic property of the as-obtained of α - Fe_2O_3 nanorod arrays obtained by using the Cl^- ion as the assistant anion is also investigated here. Part a of Figure 10 shows the temperature dependence of field-cooling (FC) magnetization of the as-synthesized α - Fe_2O_3 urchinlike nanostructure. The inserts are the corresponding differential FC curves. As it is shown in part a of Figure 10, the FC plots show a constant increase and no maximum down to 5 K. According to the differential FC curve of the sample, no Morin transition is observed for the as-synthesize flowerlike α - Fe_2O_3 . This abnormality had also been observed in the α - Fe_2O_3 nanotubes,^{23d} and mesoporous α - Fe_2O_3 with disordered walls,³⁴ which has been attributed to the presence of small crystalline particles in a few regions of the sample. Regarding the absence of the Morin transition, the shape of the M – T curve is not typical of an antiferromagnetic substance either above or below the spin-reorientation (Morin) transition. A dead surface layer of PM (paramagnetic) spins (the thickness of the layer increasing as the surface areas of the sample increased) makes it impossible to observe the intrinsic contribution (AF). Part c of Figure 10 shows the temperature dependence of FC magnetization of the α - Fe_2O_3 nanorod arrays, and the corresponding differential FC curves are displayed in the insert of part c of Figure 8, from which a sharp decrease in magnetization could be observed at about 245 K. Determined by the differential curve of FC plot, the Morin temperature of the α - Fe_2O_3 nanorod arrays is 248 K, which is lower than the bulk α - Fe_2O_3 . This could be attributed to the dislocation-free structure and small size of the α - Fe_2O_3 nanorod.

To further understand the magnetic behavior of the α - Fe_2O_3 nanostructures, magnetic hysteresis measurements of the two samples were carried out in an applied magnetic field at 5 and 300 K, with the field sweeping from -20 to 20 kOe. No saturation of the magnetization as a function of the field is observed up to the maximum applied magnetic field in both the cases. Part b of Figure 10 shows the hysteresis loops for the α - Fe_2O_3 sea urchinlike nanostructures at 5 and 300 K. The remnant magnetization and coercivity force for the α - Fe_2O_3 sea urchinlike nanostructure at 300 K are determined to be 0.0182 emu/g and 12 Oe, respectively. While at 5 K, the remnant magnetization and coercivity force for the sample are determined to be 0.144 emu/g and 115 Oe, respectively. It is easy to find that the remnant magnetization and coercivity force at 5 K are much larger than that at 300 K. The magnetization of the sample did not reach saturation under both conditions, which may indicate the disordered surface spin. Considering the porous structure of the sample, the disordered surface spin may be attributed to the adsorption of adatoms or clusters on the surfaces of the sample.³⁵ At sufficiently low temperature, the exchange interaction in each particle dominates, the surface spins become ordered, and the magnetization increases accordingly. A detailed study is still under way and will be published elsewhere. The hysteresis loops of the nanorod arrays at 5 and 300 K are displayed in part d of Figure 10. The remnant magnetization

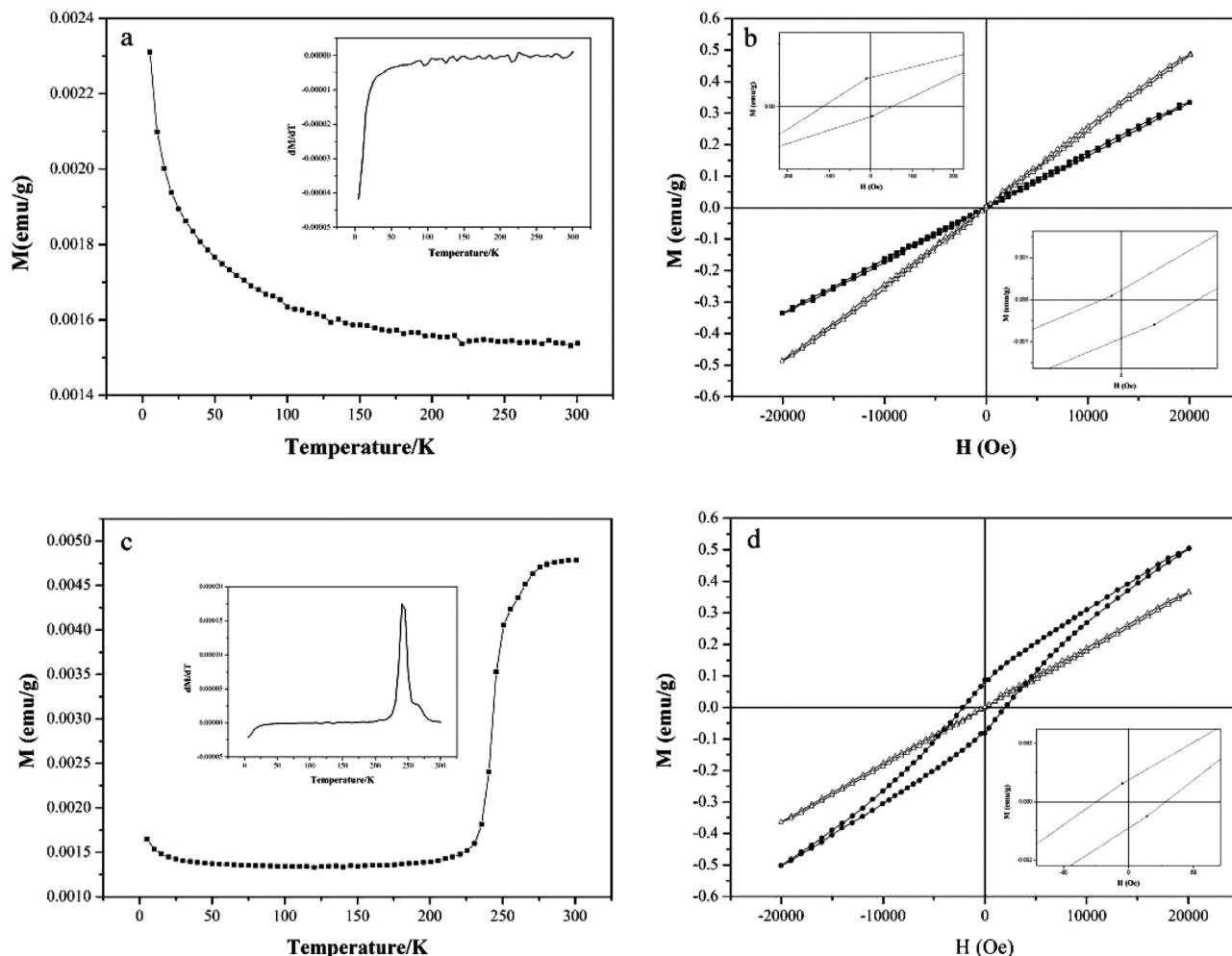


Figure 10. (a) Temperature dependence of FC magnetization for an applied field of 100 Oe for the as-prepared α - Fe_2O_3 sea urchinlike nanostructures (insert: the differential curve of the FC magnetization), (b) Magnetic hysteresis loop of the α - Fe_2O_3 sea urchinlike nanostructures at 300 K (marked as solid cubes) and 5 K (marked as triangles), (c) temperature dependence of FC magnetization for an applied field of 100 Oe for the as-prepared α - Fe_2O_3 nanorod array nanostructures (insert: the differential curve of the FC magnetization), (d) magnetic hysteresis loop of the α - Fe_2O_3 nanorod array at 300 K (marked as triangles) and 5 K (marked as solid spheres).

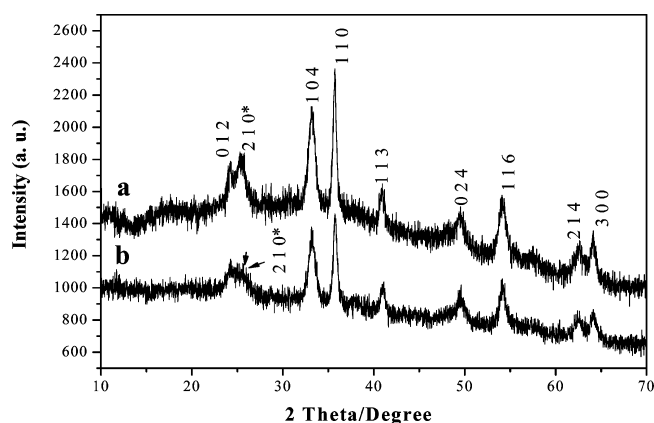


Figure 11. XRD pattern of the sea urchinlike α - Fe_2O_3 @ TiO_2 nanostructures obtained by calcining at (a) 390 °C and (b) 200 °C.

and coercivity force of the nanorod arrays are determined to be 0.089 emu/g and 2011 Oe at 5 K, respectively. However, when the temperature decreased to 5 K, the remnant magnetization and coercivity force of the nanorod arrays are determined to be 0.00079 emu/g and 44 Oe, which is much smaller than the corresponding value at room temperature. At room temperature, the remnant magnetization and coercivity force of α - Fe_2O_3 nanorod array is much larger than the sea urchinlike nanostruc-

ture. This phenomenon can be explained in two aspects: First, the shape anisotropy. It is well-known that the magnetization of materials is very sensitive to the microstructures of a particular sample.³⁶ Coercivity, as an extrinsic property of a magnet, not only depends on the spin carrier but also on the shape or the size of the magnets.³⁷ Symmetrically shaped nanoparticles, such as spheres, do not have any net shape anisotropy, and that may be the reason why the urchinlike α - Fe_2O_3 has such a low coercivity. Meanwhile, the assembly of α - Fe_2O_3 nanorods into the nanorod array results in the magnetic coupling between the nanorods, leading to higher remnant magnetization and coercivity. The magnetic hysteresis measurement of the as-sold α - Fe_2O_3 (Figure S3 of the Supporting Information) was also carried out for comparison under the same condition. SEM image (Figure S2 of the Supporting Information) shows that the as-sold α - Fe_2O_3 is mainly composed of nanospheres with diameter of about 300 nm. The remnant magnetism and coercivity are 0.0575 emu/g and 461 Oe respectively, which lies right between the values of the urchinlike and the nanorod-arrayed α - Fe_2O_3 . The nanospheres of the as-sold α - Fe_2O_3 are considered to be composed of many small particles, and the resulting crystalline anisotropy may be the main reason for the magnetic properties reported above.

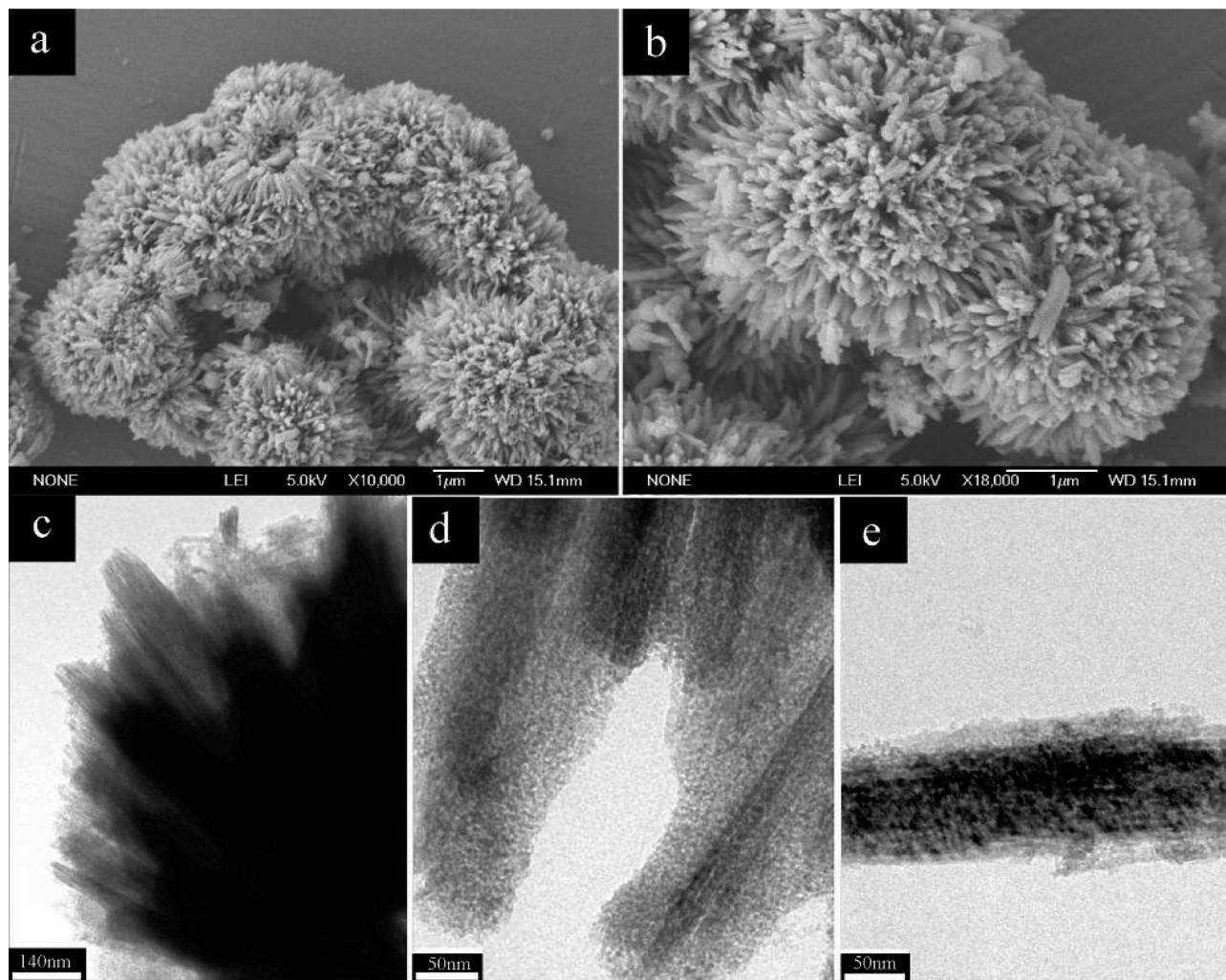


Figure 12. (a) FESEM images of the as-obtained sea urchinlike $\alpha\text{-Fe}_2\text{O}_3\text{@TiO}_2$ nanostructures by annealing at 200 °C, (b) FESEM images of the as-obtained sea urchinlike $\alpha\text{-Fe}_2\text{O}_3\text{@TiO}_2$ nanostructures by annealing at 390 °C, (c–e) low- and high-magnification TEM images of the as-obtained sea urchinlike $\alpha\text{-Fe}_2\text{O}_3\text{@TiO}_2$ nanostructures.

3.8. Characterization of the Sea Urchinlike $\alpha\text{-Fe}_2\text{O}_3\text{@TiO}_2$ Nanostructure. Part b of Figure 11 is the XRD pattern of the sea urchinlike $\alpha\text{-Fe}_2\text{O}_3\text{@TiO}_2$ nanostructures obtained by calcining at and 390 °C, which clearly indicate the presence of brookite-phased TiO_2 according to the peaks at $2\theta = 26^\circ$, termed as the (2 1 0) lattice plane of brookite (marked with asterisk). For the product obtained under 200 °C, the diffraction peak of TiO_2 is not found in the diffraction pattern (part b of Figure 11). This may be attributed to the low crystallinity of the TiO_2 , which results in the overlap of the (2 1 0) diffraction peak with the (0 1 2) diffraction peak of hematite.

Parts a and b of Figure 12 are the FESEM images of the $\alpha\text{-Fe}_2\text{O}_3\text{@TiO}_2$ nanostructures obtained by annealing the precursor at 390 °C, which clearly demonstrate that the sea urchinlike structure of $\alpha\text{-Fe}_2\text{O}_3$ was well reserved. The size of the nanostructure is little larger than the $\alpha\text{-Fe}_2\text{O}_3$ nanostructure, which may result from the coating of TiO_2 on the surface of the nanostructure. Parts c–e of Figure 12 is the TEM image of the $\alpha\text{-Fe}_2\text{O}_3\text{@TiO}_2$ nanostructures obtained by annealing the precursor at 390 °C, which shows that the surface of the sea urchinlike nanostructures are coated by a layer of TiO_2 , and the thickness of the layer is about 50 nm. The morphology of the nano composite obtained by calcining at 200 °C is similar to the product obtained by calcining at 390 °C.

Nitrogen adsorption–desorption measurement was conducted to characterize the Brunauer–Emmett–Teller (BET) surface

area and internal pore superstructure. The isotherm can be categorized as type IV, with a distinct hysteresis loop observed in the range of 0.45–1.0 P/P_0 (Figure 13). Calculated from the adsorption–desorption isotherm, the surface areas of the two samples are determined to be 58.197 and 54.887 m^2/g . Compared to the hematite nanostructure before coating, the surface areas are larger. The pore sizes of the two samples are determined to be 54 and 30 nm, according to the BJH curve of the two samples. It is worth noting that the sample obtained at 200 °C has a larger surface area than the one obtained at 390 °C, suggesting that low temperature is good for the formation improvement of surface areas.

3.9. Photocatalytic Performance of the Samples. Here, the photocatalytic performance of the as-synthesized $\alpha\text{-Fe}_2\text{O}_3$ and $\alpha\text{-Fe}_2\text{O}_3\text{@TiO}_2$ were investigated by the degradation of Rhodamine B (RB) in suspension. Part a of Figure 14 shows the evolution of the evolution of RB absorption spectra in the presence of 50 mg of $\alpha\text{-Fe}_2\text{O}_3$ sea urchinlike nanostructures, from which we can see that the concentration of RB decreased rapidly, in accordance with the photos of sample with different irradiation time (insert of part a of Figure 14). The changes in the concentration of RB under these four different situations are plotted and shown as part b of Figure 14. The concentration of RB was determined by the characteristic peak at 554 nm on the UV–vis spectra. Compared with the situation when no catalyst was added, the three samples all exhibit photocatalytic

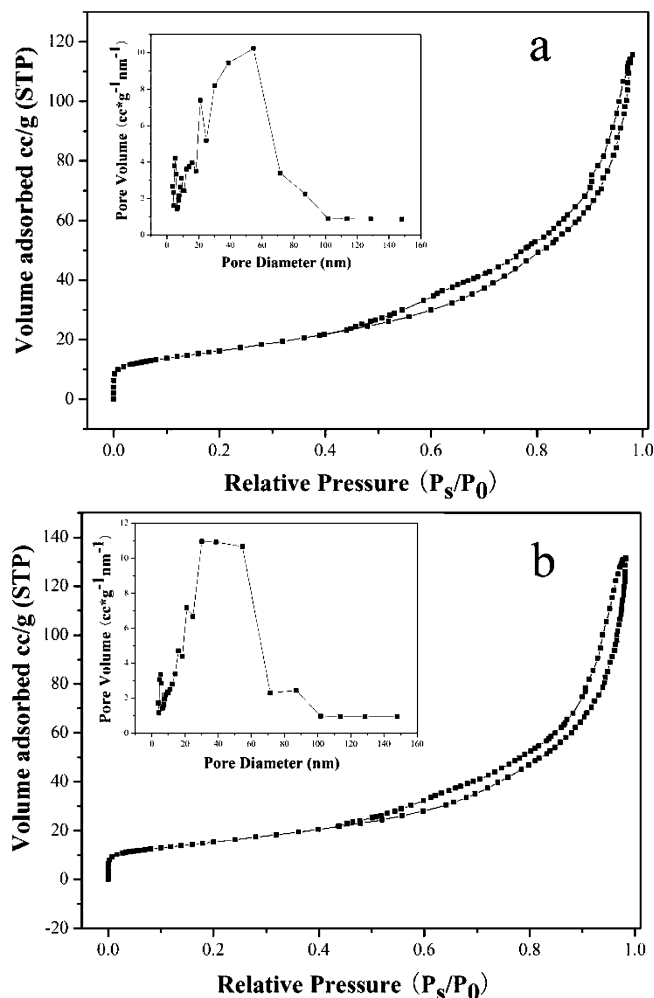


Figure 13. Nitrogen adsorption–desorption isotherm and the pore size distribution curve (insert) for the sea urchinlike $\alpha\text{-Fe}_2\text{O}_3\text{@TiO}_2$ nanostructures obtained by calcining at (a) 200 °C and (b) 390 °C.

activities. The $\alpha\text{-Fe}_2\text{O}_3\text{@TiO}_2$ nanostructures displayed higher photocatalytic activities than the as-obtained sea urchinlike hematite nanostructure, which may result from the broadening of the absorption band by TiO_2 coating. For the two samples obtained under different annealing temperature, the one obtained at lower temperature exhibits higher photocatalytic activity, which may due to the higher surface area of the sample. It is worth noting that the photocatalytic activities of the as-obtained two $\alpha\text{-Fe}_2\text{O}_3\text{@TiO}_2$ nanostructures is still lower than P25, which may result from the different crystalline phase of TiO_2 coated on the surface of hematite. This suggest that the photocatalytic activity of the $\alpha\text{-Fe}_2\text{O}_3\text{@TiO}_2$ nanostructure may be further improved by controlling the phase of TiO_2 on surface. Detailed work is underway and will be published elsewhere.

Conclusions

In summary, an inorganic anion mediated hydrothermal method was employed for the selective preparation of $\alpha\text{-Fe}_2\text{O}_3$ with novel structures. The as-prepared urchinlike $\alpha\text{-Fe}_2\text{O}_3$ are porous and constructed of well-aligned nanoneedles with an average length of up to 800 nm and a mean diameter of 150 nm; the $\alpha\text{-Fe}_2\text{O}_3$ nanorod array is composed of aligned nanorods with a mean diameter of 30 nm and a length of up to 100 nm. By applying different s into the reaction, products with different morphologies (nanocubes, nanorods, nanoplates, nanospindles, nanofibers) can be selectively synthesized. Magnetic hysteresis

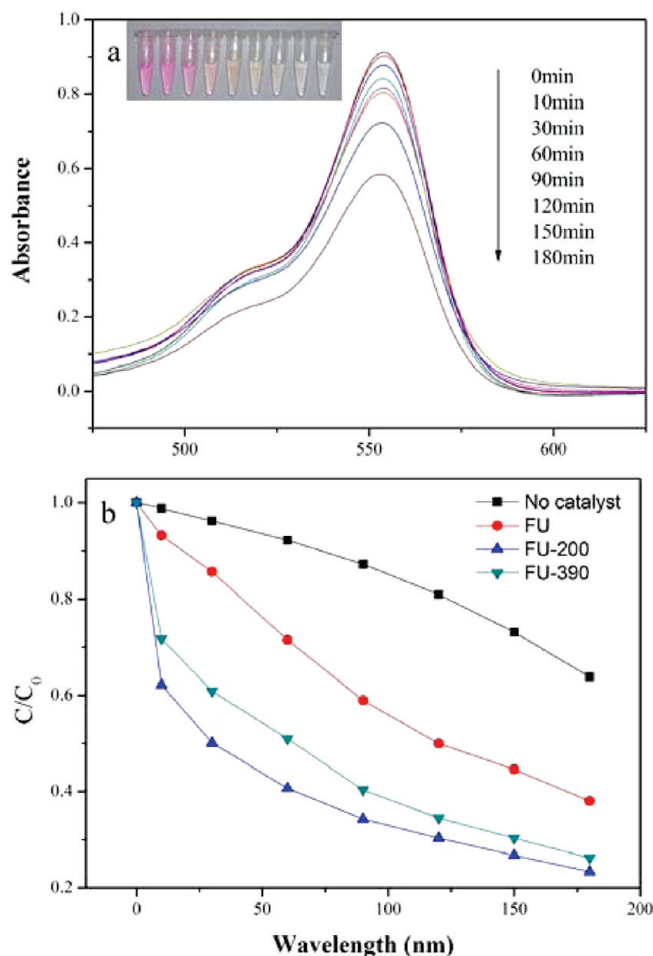


Figure 14. (a) Absorption spectra of a solution of RB (1.0×10^{-5} M, 100 mL) in the presence of 50 mg of $\alpha\text{-Fe}_2\text{O}_3$ sea urchinlike nanostructures and $\alpha\text{-Fe}_2\text{O}_3\text{@TiO}_2$ nanostructures under exposure to UV light. (b) Photocatalytic performances of various samples. (FU: $\alpha\text{-Fe}_2\text{O}_3$ sea urchinlike; FU-200: $\alpha\text{-Fe}_2\text{O}_3\text{@TiO}_2$ nanostructures by annealing at 200 °C; FU-390: $\alpha\text{-Fe}_2\text{O}_3\text{@TiO}_2$ nanostructures by annealing at 390 °C; C: the concentration of RB at designated time; C_0 : the initial concentration of RB).

measurements reveal that magnetic properties of the as-obtained products were shape-dependent. The as-obtained $\alpha\text{-Fe}_2\text{O}_3$ nanostructures show photocatalytic activity on the decomposition of RhB upon irradiation by the UV light. Moreover, this facile synthetic route, free of template and capping agent, can be easily controlled to prepare such unique structures and hence is expected to be applicable to the preparation of other nanomaterials.

Acknowledgment. Financial support by the National Natural Science Foundation of China, the 973 Projects of China (No. 20621061), and the Program for New Century Excellent Talents in university (NCET) are gratefully acknowledged.

Supporting Information Available: EDS spectrum of the as-obtained hematite nanostructures, SEM image, and M-H curve of the as-sold hematite. This material is available free of charge via the Internet at <http://pubs.acs.org>.

References and Notes

- (1) Hu, J. T.; Odom, T. W.; Lieber, C. M. *J. Am. Chem. Soc.* **1999**, *121*, 435.
- (2) Law, M.; Goldberg, J.; Yang, P. D. *Annu. Rev. Mater. Res.* **2004**, *34*, 83.

- (3) Yuan, J. K.; Li, W. N.; Gomez, S.; Suib, S. L. *J. Am. Chem. Soc.* **2005**, *127*, 14184.
- (4) Liu, B.; Zeng, H. C. *J. Am. Chem. Soc.* **2004**, *126*, 8124.
- (5) Shen, G. Z.; Bando, Y.; Golberg, D. *Appl. Phys. Lett.* **2006**, *88*, 123107.
- (6) Li, X. H.; Zhou, B.; Pu, L.; Zhu, J. J. *Cryst. Growth. Des.* **2008**, *8*, 771.
- (7) Narayanaswamy, A.; Xu, H. F.; Pradhan, N. *J. Am. Chem. Soc.* **2006**, *128*, 10310.
- (8) Ni, X. M.; Zhao, Q. B.; Zhang, D. E.; Zhang, X. J.; Zheng, H. G. *J. Phys. Chem. C* **2007**, *111*, 601.
- (9) Faust, B. C.; Hoffmann, M. R.; Bahnmann, D. W. *J. Phys. Chem.* **1989**, *93*, 6371.
- (10) Han, J. S.; Bredow, T.; Davey, D. E.; Yu, A. B.; Mulcahy, D. E. *Sens. Actuators, B* **2001**, *75*, 18.
- (11) Chen, J.; Xu, L.; Li, W.; Gou, X. *Adv. Mater.* **2005**, *17*, 582.
- (12) (a) Matijević, E.; Scheiner, P. *J. Colloid Interface Sci.* **1976**, *61*, 24. (b) Hamada, S.; Matijević, E. *J. Chem. Soc., Faraday Trans. 1* **1982**, *78*, 2147. (c) Ozaki, M.; Kratochvil, S.; Matijević, E. *J. Colloid Interface Sci.* **1984**, *102*, 146. (d) Ozaki, M.; Ookoshi, N.; Matijević, E. *J. Colloid Interface Sci.* **1990**, *137*, 546. (e) Sugimoto, T.; Khan, M.; Muramatsu, A. *Colloids Surf., A* **1993**, *70*, 167. (f) Lu, J.; Chen, D. R.; Jiao, X. L. *J. Colloid Interface Sci.* **2006**, *303*, 437. (g) Tang, B.; Wang, G. L.; Zhuo, L. H.; Ge, J. C.; Cui, L. J. *Inorg. Chem.* **2006**, *45*, 5196. (h) Wu, C. Z.; Yin, P.; Zhu, X.; Ouyang, C. Z.; Xie, Y. *J. Phys. Chem. B* **2006**, *110*, 17806.
- (13) Wen, X. G.; Wen, S. H.; Dong, Y.; Wang, Z. L.; Yang, S. H. *J. Phys. Chem. B* **2005**, *109*, 215.
- (14) Zhao, Y. M.; Li, Y. H.; Ma, R. Z. *Small* **2006**, *2*, 422.
- (15) Xue, D. S.; Gao, C. X.; Liu, Q. F.; Zhang, L. Y. *J. Phys.: Condens. Matter* **2003**, *15*, 1455.
- (16) Jiao, F.; Yue, B.; Zhu, K. K.; Zhao, D. Y.; He, Y. *Chem. Lett.* **2003**, *32*, 771.
- (17) Li, S. Z.; Zhang, H.; Wu, J. B.; Ma, X. Y.; Yang, D. R. *Cryst. Growth Des.* **2006**, *6*, 351.
- (18) Zhong, L. S.; Hu, J. S.; Liang, H. P.; Cao, A. M.; Song, W. G.; Wan, L. J. *Adv. Mater.* **2006**, *18*, 2426.
- (19) Zhang, W.; Chen, J.; Wang, X.; Qi, H. L.; Peng, K. S. *Appl. Organomet. Chem.* **2009**, *23*, 200.
- (20) Cao, M. H.; Liu, T. F.; Gao, S.; Sun, G. B.; Wu, X. L.; Hu, C. W.; Wang, Z. L. *Angew. Chem., Int. Ed.* **2005**, *44*, 4197.
- (21) Zhu, L. P.; Xiao, H. M.; Liu, X. M.; Fu, S. Y. *J. Mater. Chem.* **2006**, *16*, 1794.
- (22) Zhong, X. L.; Song, J. M.; Zhang, S.; Yao, H. B.; Xu, A. W.; Yao, W. T. *J. Phys. Chem. C* **2008**, *112*, 11916.
- (23) (a) Yin, Y.; Alivisatos, A. P. *Nature* **2005**, *437*, 664. (b) Cao, M.; Hu, C.; Peng, G.; Qi, Y.; Wang, E. *J. Am. Chem. Soc.* **2003**, *125*, 4982. (c) Pileni, M. P. *Nat. Mater.* **2003**, *2*, 145. (d) Liu, L.; Kou, H. Z.; Mo, W. L.; Liu, H. J.; Wang, Y. Q. *J. Phys. Chem. B* **2006**, *110*, 15218.
- (24) (a) Liu, Y.; Chu, Y.; Zhuo, Y.; Li, M.; Li, L.; Dong, L. *Cryst. Growth Des.* **2007**, *7*, 467. (b) Houtepen, A. J.; Koole, R.; Vanmaekelbergh, D.; Meeldijk, J.; Hickey, S. G. *J. Am. Chem. Soc.* **2006**, *128*, 6792. (c) Wiley, B.; Herricks, T.; Sun, Y.; Xia, Y. *Nano Lett.* **2004**, *4*, 1733. (d) Wang, W. S.; Zhen, L.; Xu, C. Y.; Shao, W. Z. *Cryst. Growth Des.* **2009**, *9*, 1558.
- (25) Sugimoto, T.; Wang, Y.; Itoh, H.; Muramatsu, A. *Colloids Surf., A* **1998**, *134*, 265.
- (26) (a) Matijević, E.; Sheiner, P. *J. Colloid Interface Sci.* **1980**, *74*, 405. (b) Hamada, S.; Matijević, E. *J. Colloid Interface Sci.* **1981**, *84*, 274.
- (27) Zeng, S. Y.; Tang, K. B.; Liang, Z. H.; Wang, D.; Wang, Y. K.; Zhou, W. W. *J. Phys. Chem. C* **2007**, *111*, 10217.
- (28) Dousma, J.; Den Ottelander, D.; De Bruyn, P. L. *J. Inorg. Nucl. Chem.* **1979**, *41*, 1565.
- (29) Cornell, R. M.; Schwertmann, U. *The Iron Oxides. Structure, Properties, Reactions, Occurrence and Uses*, VCH: Weinheim, 1996.
- (30) (a) Pauly, T. R.; Liu, Y.; Pinnavaia, J.; Billinge, L.; Bieker, T. P. *J. Am. Chem. Soc.* **1999**, *121*, 8835. (b) Zhang, L. Z.; Yu, J. C. *Chem. Commun.* **2003**, 2078. (c) Wong, S. T.; Lin, H. P.; Mou, C. Y. *Appl. Catal., A* **2000**, *198*, 103.
- (31) Rolison, D. R. *Science* **2003**, *299*, 1698.
- (32) Amin, N.; Arajs, S. *Phys. Rev. B* **1987**, *35*, 4810.
- (33) (a) Zeng, S. Y.; Tang, K. B.; Li, T. W. *J. Colloid Interface Sci.* **2007**, *312*, 513. (b) Zeng, S. Y.; Tang, K. B.; Liang, Z. H.; Wang, D.; Wang, Y. K.; Zhou, W. W. *J. Phys. Chem. C* **2008**, *112*, 4836.
- (34) Jiao, F.; Harrison, A.; Jumas, J. C.; Chadwick, A. V.; Kockelmann, W.; Bruce, P. G. *J. Am. Chem. Soc.* **2006**, *128*, 5468.
- (35) Zhao, Y. M.; Charles, W. D.; Gregory, D. H.; Kockenberger, W.; Liu, Y. H.; Hu, W. B.; Ahmad, I.; McCartney, D. G. *Chem. Mater.* **2007**, *19*, 916.
- (36) Sorescu, M.; Brand, R. A.; Mihaila-Tarabasanu, D.; Diamandescu, L. J. *Appl. Phys.* **1999**, *85*, 5546.
- (37) Sun, H. L.; Shi, H. T.; Zhao, F.; Qi, L. M.; Gao, S. *Chem. Commun.* **2005**, *34*, 4339.

JP909111J